ADVANCED MATERIALS INTERFACES
www.advmatinterfaces.de

Nickel Quantum Dots Anchored in Biomass-Derived Nitrogen-Doped Carbon as Bifunctional Electrocatalysts for Overall Water Splitting

Shuang Chen, Xin Min, Yajing Zhao, Xiaoxian Wu, Dan Zhang, Xifeng Hou, Xiaowen Wu, Yan'gai Liu, Zhaohui Huang, Amr. M. Abdelkader, Kai Xi,* and Minghao Fang**

Quantum dots (QD), mixed with carbon materials, have gained increasing interest in the last few years as electrocatalysts due to their outstanding properties, such as excellent catalytic activity and good thermodynamic stabilities. However, most QD-carbon hybrids show lower catalytic activities than that theoretically predicted due to the aggregation of the QD-carbon nanostructures during processing. Herein, biomass is used as a carbon source to prepare QD carbon nanostructures (Ni@C—N) to address the aforementioned issue. The cells walls and membranes in the biomass materials are usually rich in sites that could regulate the deposition and growth of Ni from a salt precursor by a simple solution impregnation method. Due to the abundance of the seeding sits and the limited supply of Ni^+, the Ni particles size is restricted to the QD level with 3–4 nm. The formed Ni compounds QD are strongly linked to the cells walls and membranes, which could be maintained after subsequent heat treatment. The prepared 3D architecture has high catalytic activity, large surface area, strong physical integration, and rapid charge transfer capability, which collectively enhances the performance toward oxygen evolution reaction and hydrogen evolution reaction, opening the door to empower the next-generation green fuel conversion for carbon neutral.

1. Introduction

Hydrogen is considered a promising clean energy carrier to satisfy the growing energy demands and fulfill the goal of reducing carbon emissions.[1–3] As an alternative to gray hydrogen, where hydrogen is produced by cracking hydrocarbon gases at high temperatures, green hydrogen is produced by the electrolysis of water in what is known as water splitting.[4–6] In the electrochemical water splitting, hydrogen is produced at the cathodic through hydrogen evolution reaction (HER), and anodic oxygen evolution reaction (OER) produces pure oxygen.[7–10] The process requires the use of efficient electrocatalysts, such as the Pt HER catalyst, and the IrO_2 and RuO_2 OER catalysts.[11–16] Despite development in producing and enhancing the performance of these noble metals or rare earth compounds, the majority of the water-splitting cost is still the cost of electrocatalysts.[17–21] It is important to develop efficient nonprecious metals' bifunctional electrocatalysts for HER and OER in the same electrolyte.[22,23]

As an alternative to the expensive noble and rare earth metals, the transition metal compounds have been used successfully in recent years. Metallic Ni, Co, Fe, and their oxides, chalcogenides, carbides, selenides, and phosphides, have garnered particular attention due to their good electrocatalytic performances for HER and

S. Chen, X. Min, Y. Zhao, X. Wu, Y. Liu, Z. Huang, M. Fang
Beijing Key Laboratory of Materials Utilization of Nonmetallic Minerals and Solid Wastes
National Laboratory of Mineral Materials
School of Materials Science and Technology
China University of Geosciences
Beijing 100083, China
E-mail: minx@cugb.edu.cn; fmh@cugb.edu.cn

X. Min, D. Zhang
State Key Laboratory of Mineral Processing
Beijing General Research Institute of Mining and Metallurgy
Beijing 100070, China

X. Min, X. Wu
Engineering Research Center of Non-metallic Minerals of Zhejiang Province
Zhejiang Non-metallic Mineral Research Institute
Hangzhou 310007, China

X. Hou
TongLing Boya Duye New Material Technology Co. Ltd.
Tongling 244000, China

A. M. Abdelkader
Faculty of Science and Technology
Bournemouth University
Talbot Campus
Fern Barrow
Poole BH12 5BB, UK

K. Xi
Xi'an Key Laboratory of Sustainable Energy Materials Chemistry
School of Chemistry
Xi'an Jiaotong University
Xi'an 710049, China
E-mail: kx210@cam.ac.uk

The ORCID identification number(s) for the author(s) of this article can be found under https://doi.org/10.1002/admi.202102014.

DOI: 10.1002/admi.202102014

OER, which are comparable to that of Pt-based catalysts.[24–30] However, most transition-metal-based compounds have relatively low electrical conductivity, limiting the charge transfer, and weaken their electrocatalytic activity. A common concept to improve the conductivity is by mixing or coating the transition metal compounds with carbon nanomaterials to form conductive electrocatalysts.[31–33] These composite electrocatalysts are intensively studied, yet show high overpotential and poor stability for HER and OER.[34,35] It is commonly believed that the catalytic activity is originated from moderate bonding energy between the proton and hydride acceptor sites on the surface of the electrocatalyst and the reaction intermediates in water splitting. Nevertheless, the metallic nanocatalysts tend to form agglomerates or polydisperse of varying sizes regardless of the synthesis methods due to their high surface energy.[36–38] This covers a significant part of the electrocatalyst surface and changes the bonding energy with the intermediates, reducing or even passivating the catalytic activities. Also, the particle aggregation during the electrode fabricating weakens the contact between catalysts and substrates and might lead to peeling the metal catalysts during the water splitting.[39–41] The unstable electrode might also suppress the catalytic reaction on the catalyst surface owing to the tough electron penetration, further limiting their applications.[38,42–44] Therefore, despite the reported significant progress, it is important to develop efficient transition metal catalysts strongly immobilized on carbon matrix through a simple, controllable, and scalable synthesis method.

Herein, we present a concept to fabricate Ni quantum dots (QDs) anchored on 3D honeycomb-like N-doped carbon (Ni@C—N) bifunctional nanocatalysts through a simple solution impregnation followed by an annealing step. The N-doped carbon (C—N) works mainly as a backbone to support the Ni QD but also provides the nanocatalysts with good electrical conductivity, fast charge transport, and unique 3D morphology with a high surface area. Due to the confinement effect originated from the strong chemical bonding between the Ni ions and cell wall or membrane in biomass raw materials, the as-prepared Ni nanocrystals are restricted to the QD size of about 3–4 nm, much smaller than that reported in the literature for Ni–carbon composites. The synergy between the catalytically active QD and the multifunction N–C backbones provides Ni@C—N with a unique set of properties that promote efficient electrocatalytic processes. Furthermore, the strong chemical bond between the Ni QD and the C—N support facilitates the charge transfer and provides good long-term stability. Besides, this new method is also simple, controllable, low cost, and environmentally friendly. Thus, the new concept offers a promising strategy for fabricating various non-noble metal electrocatalysts in fuel cells, energy storage, chemical industry, petrochemical, biochemical, and environmental protection fields.

2. Results and Discussion

2.1. Design of the Ni@C—N Composite Nanocatalysts

A schematic diagram of the synthesis process of Ni@C—N is shown in **Figure 1**a. First, the biomass materials, asparagus (AG), white radish (WR), and potato (PT), were impregnated with $Ni(NO_3)_2$ aqueous solution for 2 h, and subsequently freeze-dried to obtain the green precursor. The green precursor was then annealed at 800 °C in an Ar atmosphere to obtain the nickel QD supported on N-doped bioderived carbon. For comparison, we also prepared Ni-free N-doped carbon material (C—N—AG) by impregnating the biomass materials in deionized water for 2 h. The synthesis mechanism of Ni@C—N samples can be understood from the structure and composition of plant cells and by taking AG as an example. When the AG is impregnated into the $Ni(NO_3)_2$ solution, Ni^{2+} ions first diffuse and penetrate through the cell membrane; then ion exchange occurs between Ni^{2+} ions and cellulose (and phospholipid molecule or membrane protein) in the cell wall or membrane, as shown in Equations (S1)–(S3) (Supporting Information), respectively. As a result of the ion-exchange process, most Ni^{2+} ions are discharged and grow to form Ni-containing nanoparticles (NPs) bonded to the cells' surface of the cell wall and membrane. Following the freeze-drying desiccation process, the honeycomb structure of natural AG could be maintained, and the Ni-containing nanoparticles are still uniformly deposited on the cell wall and membrane. The carbon from the biomass source reduces Ni-containing nanoparticles into metallic Ni nanoparticles (or QD) during the annealing step. In the meantime, N and C from the biomass raw materials react to form the C—N backbone supports. The annealing process does not harm the original bond between Ni^{2+} ions and the cell wall, meaning stable chemical bonds are exist between the formed Ni nanoparticles and C—N. Since there are numerous active sites for the Ni^{2+} ions' deposition, the number of ions available per site is limited, which also controls the particles' growth. The uniform distribution of the active growth sites also satisfies the Ni particles' homogeneous distribution and prevents their aggregation. This suggested mechanism finds some supporting evidence from the structural and chemical analyses of the produced composite, as discussed in the following sections.

2.2. Morphology and Structure of Ni@C—N Electrocatalysts

Despite the different biomass sources, all the produced materials showed almost the same honeycomb for the carbon backbone (Figure 1b,f,j; Figure S1, Supporting Information). This unique 3D architecture is composed of very thin connected carbon walls, giving a high specific surface area of 233.3 $m^2\ g^{-1}$ after annealing (Figure S2 and Table S2, Supporting Information). The pyrolysis of the hydrocarbon and the volatile materials' release during the annealing produce macropores and micropores of different sizes. The magnified transmission electron microscope (TEM) and high-resolution transmission electron microscope (HRTEM) detected quantum dots of the size 3–7 nm uniformly distributed on the surface of C—N layers, with almost no aggregation or agglomeration (Figure 1c,d,g,h,k,l; Figure S3, Supporting Information). The interlayer distance measured from lattice fringes (Figure 1e,i,m) are about 0.203 nm, typical for the (111) plane of metallic Ni. The Ni nanocatalysts' selected-area electron diffraction (SAED) patterns (Figure S4, Supporting Information) are also in line with the HRTEM results. The X-ray diffraction (XRD) analysis

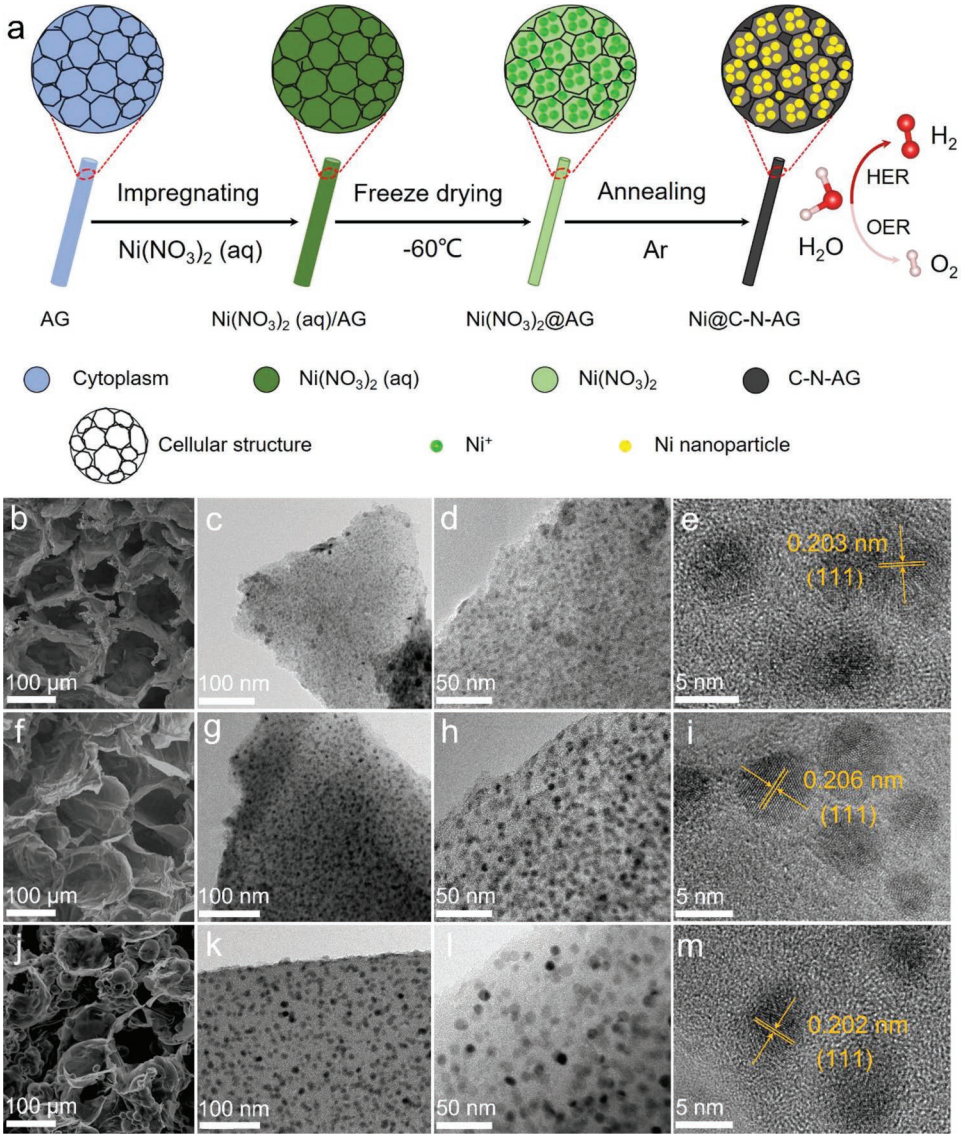

Figure 1. a) Schematic diagram for the preparation process of Ni@C—N nanocomposites, using the biomass material AG as an example. b–m) The morphology of Ni@C—N nano-electrocatalysts. SEM images of b) Ni@C—N—AG, f) Ni@C—N—WR, and j) Ni@C—N—PT; TEM images in different magnifications of c,d) Ni@C—N—AG, g,h) Ni@C—N—WR, and k,l) Ni@C—N—PT; HRTEM images of e) Ni@C—N—AG, i) Ni@C—N—WR, and m) Ni@C—N—PT.

also confirms the crystallinity of the Ni particles, with diffraction peaks at 44.5°, 52.0°, and 76.2° corresponding to the (111), (200), and (220) lattice planes of cubic-structured Ni (**Figure 2**a; Figure S5, Supporting Information). Interestingly, the particle size of the formed Ni QD differs with respect to the type of biomass raw materials, suggesting that the composition and structure of the biomass might play an important role in the growth of the Ni QD. Nevertheless, the size of Ni nanoparticles in Ni@C—N—AG composite is much smaller than reported literature (about 7–50 nm), which is critical for the exposure of active catalytic sites.[45] The energy dispersive spectroscopy (EDS) analysis further confirms the uniform distribution of Ni QD alongside other elements such as N, O, and C (Figure S6, Supporting Information). The graphitization of the N-doped carbon backbone of the composite is first confirmed by the XRD, where a broad diffraction peak can be observed at 26.4° in the pattern of the C—N—AG controlled samples. The Raman spectroscopic analysis further confirms the graphitization, as shown in Figure 2b. The peak that appears at 1580 cm^{-1} (G band) in all samples' spectra is attributed to the graphitic sp^2 carbon (E_{2g}). The other peaks in the spectra are the D1 at around 1350 cm^{-1} band for the disordered sp^3 carbon defects (A_{1g}), the D3 band for amorphous carbon, and the D4 band for the polyene-like carbon structures or ionic impurities.[46] The intensity ratio of the D1 and G bands (I_{D1}/I_G) decreases with the increasing temperature (Figures S7 and S8, and Table S3, Supporting Information), suggesting the enhancing graphitic structure of the C—N matrix at high temperature. The strong bonding between Ni QD and the N-doped carbon backbones is first confirmed extensive sonication for 1 h. No apparent changes are observed after

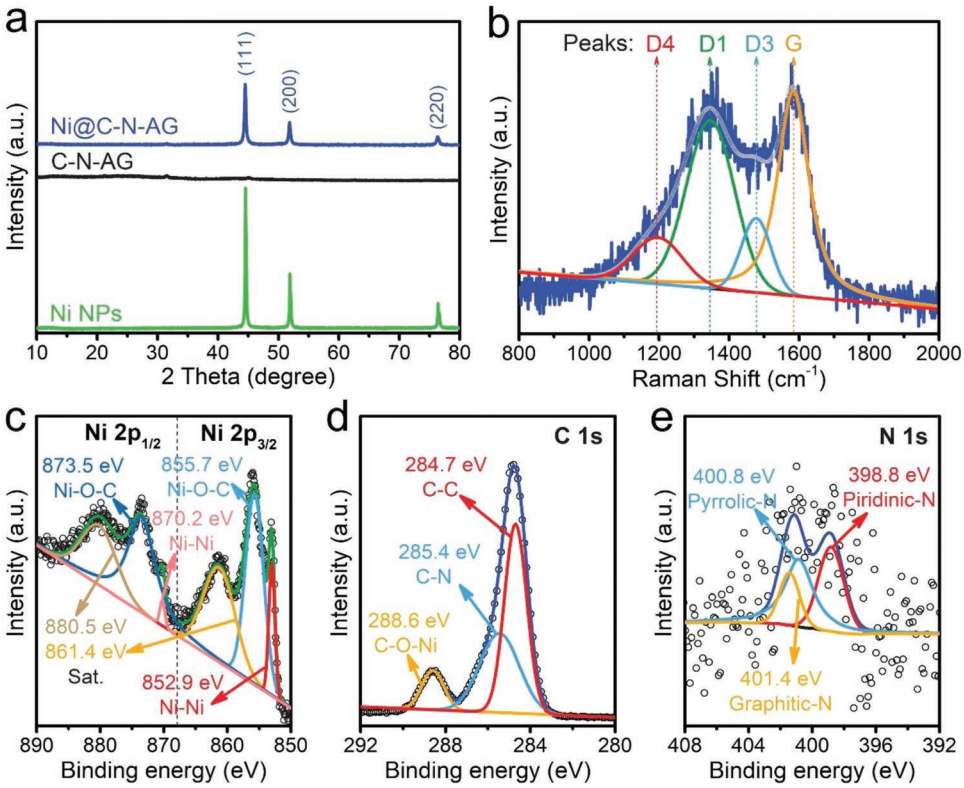

Figure 2. The structure of Ni@C−N−AG nano-electrocatalysts. a) XRD patterns of Ni@C−N−AG, C−N−AG, Ni nanoparticles (Ni NPs). b) Curve fitting of the Raman spectrum of Ni@C−N−AG; c–e) High-resolution XPS spectra of c) Ni 2p, d) C 1s, and e) N 1s of Ni@C−N−AG. It should be noted that the Ni $2p_{3/2}$ band shows peaks at 852.9 and 855.7 eV along with one shakeup satellite peak at 861.4 eV, while the Ni $2p_{1/2}$ spectrum exhibits two peaks at 870.2 and 873.5 eV with a satellite peak at 880.5 eV.

sonication, as shown by the TEM images in Figure S9 (Supporting Information). The strong adhesion between Ni QD and C−N is beneficial for the electron-transfer capability and the long-term electrocatalytic stability.

Moreover, the X-ray photoelectron spectroscopy (XPS) was performed to analyze the surface element composition and valence states in the Ni@C−N−AG composite. The survey XPS spectrum reveals the presence of Ni, C, N, and O elements (Figure S10, Supporting Information) with no obvious impurity, consistent with the energy dispersive X-Ray Spectroscopy (EDX) and XRD results. In the high-resolution Ni 2p spectrum, as shown in Figure 2c, the peaks at 853.0 and 870.2 eV are ascribed to Ni^0 species from the Ni−Ni metallic bond in Ni nanoparticles.[47] The peaks at 855.7 and 873.4 eV correspond to the oxidized Ni species,[48] most likely formed by the surface oxidation of Ni QD. The absence of any signs for Ni−O compounds in the XRD patterns suggested that the oxidation is limited to the QD surface. Detecting different Ni valences in the same nanoparticles suggests different functional groups and stoichiometry of Ni−O, which is beneficial for the electrocatalytic HER performance.[27,49] The deconvoluted high-resolution spectrum of C 1s reveals peaks for the C−C (284.7 eV), C−N (285.4 eV), and C−O−Ni (288.6 eV) species (Figure 2d).[50] Detecting the peak at 288.6 eV C−O−Ni provides evidence that the interactions between Ni QD and the N-doped carbon go beyond the weak physical attachments to a strong chemical bond, which is beneficial for long cycle life. The N 1s spectrum is deconvoluted into three characteristic peaks at 398.8, 400.8, and 401.4 eV, which are attributed to pyridinic N, pyrrolic N, and graphitic N, respectively (Figure 2e).[43] The high-resolution XPS spectra of C 1s and N 1s further confirm the incorporation of nitrogen element in the carbon matrix,[51] which could also facilitate the bonding between the Ni nanoparticles and the C−N layer. Our density functional theory (DFT) calculation (Figure S11, Supporting Information) suggested that the pyridinic N is preferential to link N with the Ni, forming highly active Ni−N sites for various electrocatalytic processes.[52] The content of N is quantitatively calculated to be about 0.23 at%, and the atomic ratio of Ni:C in the Ni@C−N−AG sample is found to be 3.38:1 (Table S4, Supporting Information), which is well consistent with the Ni loading amount of 42.6 wt% measured by inductively coupled plasma optical emission spectroscopy (ICP-OES).

2.3. Electrochemical Performances

The HER and OER activities were investigated via a three-electrode system in 1.0 M KOH solution. First, the HER performances as the functions of immersion solution concentration and annealing temperature were evaluated. The best HER activity is obtained at the $Ni(NO_3)_2$ solution concentration of 0.3 M and the annealing temperature of 800 °C (Figures S12 and S13, and Table S5, Supporting Information) suggesting

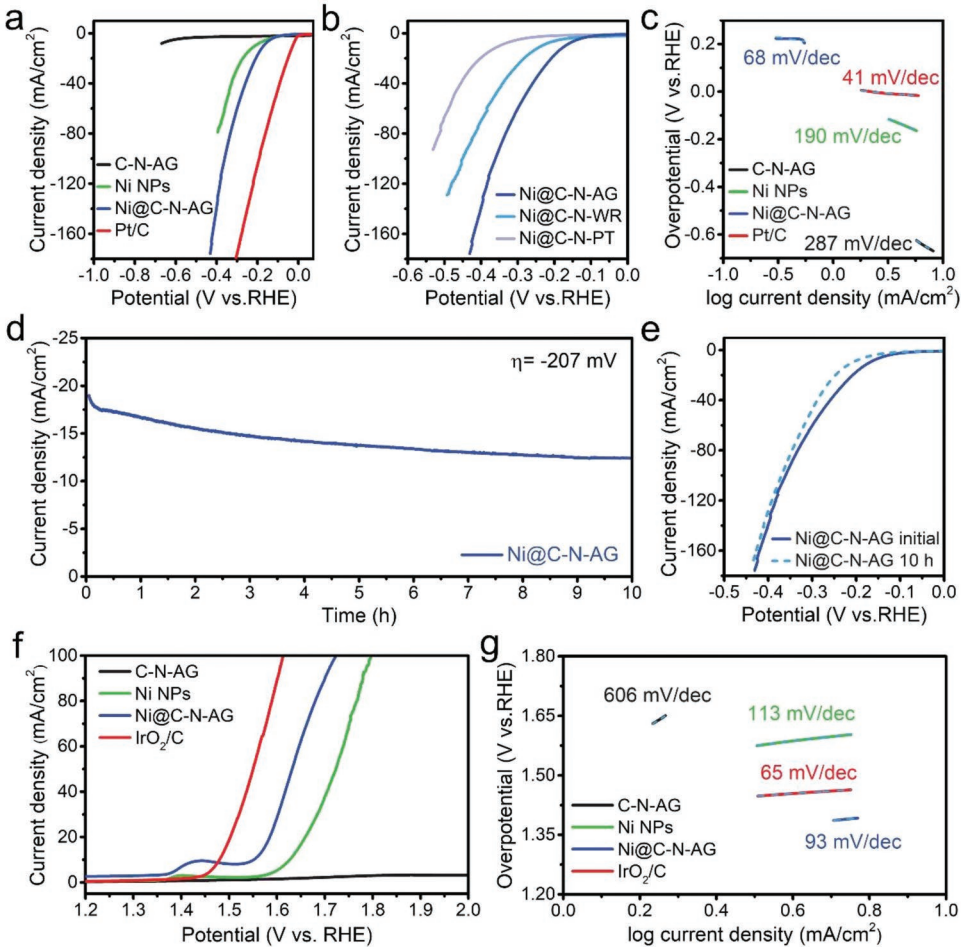

Figure 3. Electrochemical performance of Ni@C—N—AG in 1.0 M KOH solution. a) HER polarization curves of C—N—AG, Ni NPs, Ni@C—N—AG, and Pt/C. b) HER polarization curve of Ni@C—N—AG, Ni@C—N—WR, and Ni@C—N—PT. c) Tafel plots obtained from the linear sweep voltammetry (LSV) polarization curves in panel (a). d) Chronoamperometric curve of Ni@C—N—AG at the overpotential of –207 mV for 10 h. e) LSV curves of Ni@C—N—AG before and after 10 h of chronoamperometry. f) OER polarization curves of C—N—AG, Ni NPs, Ni@C—N—AG, and IrO_2/C. g) Tafel plots for the OER LSV curves in panel (f).

that these conditions are optimum to synthesis efficient structures for electrocatalysts. Furthermore, various loadings of the active materials ranged from 0.2 to 1.25 mg cm^{-2} were cast on the glassy carbon current collector. The optimum loading was found to be 1.25 mg cm^{-2} (Figure S14 and Table S6, Supporting Information), and hence the electrodes used for the rest of the electrochemical investigation are all fabricated and tested at these conditions. For comparison, we also investigated other electrodes' catalytic performance, including commercial 20 wt% Pt/C, Ni NPs, and C—N—AG for HER, as shown in **Figure 3**a. Commercial Pt/C catalyst exhibits the highest activities for HER with an overpotential of 27 mV at the current density of 10 mA cm^{-2}, way less than the overpotential of both the Ni-free C—N—AG and commercial Ni NPs. By anchoring the Ni QD on the C—N—AG backbone, the as-prepared Ni@C—N—AG exhibits high HER activity with a low onset potential of 86 mV.[39,53] Only 170 mV is needed to achieve a current density of 10 mA cm^{-2} for Ni@C—N—AG, and the overpotentials to produce current densities of 50, 100, and 180 mA cm^{-2} are 280, 360, and 430 mV, respectively. These results indicated that the synergy between Ni QD and the N-doped carbon porous backbone facilitates the catalytic process with overpotentials in KOH alkaline electrolyte lower or comparable with the most active Ni-based and non-noble-based catalysts.[40,54] Under the same condition, the initial overpotential recorded for the Ni@C—N—AG electrode is lower than any reported bio-derived C—N composite reported in the literature (Figure 3b; Table S7, Supporting Information).[16,55–57] The Tafel slope of Ni@C—N—AG is 68 mV dec^{-1}, which is close to that of the commercial Pt/C (41 mV dec^{-1}), and far below the Ni NPs (190 mV dec^{-1}) (Figure 3c; Table S8, Supporting Information). This result indicates that the HER process occurs through a Volmer–Heyrovsky mechanism, which signifies rate-limiting electrochemical recombination with an additional proton after a fast discharge of a proton. The relatively small Tafel slope for Ni@C—N is also satisfying to acquire a sizeable current density at low overpotential, confirming the high activity toward HER. It is suggested that the increased activity is ascribed to the large specific surface area and the availability of numerous sites for electrocatalysis. Besides, the graphitized 3D C—N matrix

promotes the charge transfer in the Ni@C—N catalyst, further enhances the overall HER activity. The electrochemical stability of Ni@C—N—AG is investigating by a long-term chronoamperometry method in a 1.0 M KOH solution. After 10 h of electrolysis at a constant potential of –207 mV, no significant current decay can be observed (Figure 3d). Furthermore, the polarization curve shifts negligibly at a higher current density of 175 mA cm^{-2} (Figure 3e), suggesting good electrochemical stability for HER catalysis in alkaline solution. The TEM image of the sample after the long-term HER process shows almost no changes in the original structure of Ni@C—N, confirming the excellent stability of the prepared composite as a result of the strong bonds between Ni QD and the C—N backbone (Figure S15, Supporting Information).

We then evaluated the catalytic activity of Ni@C—N—AG toward OER in the same setup with 1.0 M KOH electrolyte. Electrodes fabricated using commercial IrO_2/C, Ni NPs, and C—N—AG are also examined for comparison. As shown in Figure 3f, without Ni QD, the C—N—AG network exhibits nearly no OER activity. Commercial IrO_2/C offers the best OER performance when the produced current density is higher than 10 mA cm^{-2}. However, at a current density lower than 10 mA cm^{-2}, Ni@C—N—AG performs better than other tested electrodes with the lowest overpotential of 319 mV. The overpotentials of 353, 400, and 492 mV are required to yield the current densities of 20, 50, and 100 mA cm^{-2}, comparable with that required by the IrO_2/C and outperformed other Ni/carbon composites in the literature (Tables S8 and S9, Supporting Information). The Tafel slope of Ni@C—N—AG is calculated to be 93 mV dec^{-1}, which is closed to the commercial IrO_2/C and much lower than Ni NPs (Figure 3g; Table S8, Supporting Information), indicating a fast OER catalytic kinetic for Ni@C—N—AG. Finally, the HER and OER activities of Ni@C—N—AG are compared with those of some state-of-the-art non-noble metal-based bifunctional electrocatalysts, as shown in Table S10 (Supporting Information). The HER and OER performances of Ni@C—N—AG catalyst at 10 mA cm^{-2} are comparable to those of other bifunctional electrocatalysts in alkaline media. The high catalytic activities, long-life stability coupling with the cheap and sustainable precursor, make the Ni@C—N electrodes excellent candidates for practical application for water splitting.[58]

2.4. DFT Calculations

The overall water-splitting reaction mechanism in alkaline solutions is proposed in **Figure 4**a and Figure S16 (Supporting Information), in which the OER process involves four steps, namely, OH^-, OH_{ads}, O_{ads}, and OOH_{ads}.[59] The HER consists of electrochemical hydrogen adsorption (Volmer reaction) and chemical desorption (Tafel reaction).[60] The specific reaction pathway includes H_2O adsorption, the electrochemical dissociation of adsorbed H_2O into adsorbed OH^- and H^+, the OH^- desorption to refresh the surface, and the H_2 formation.[61] First-principles DFT calculations could shade more light on the HER activity of Ni@C—N in the alkaline solution and the role of the active sites. The binding energies of H_2O, H^+, and OH^-, as well as H_2O dissociation on the Ni_{13}@C—N, Pt_{13}, Ni_{13}, and C—N surfaces, were explored (Figure 4b–e; Figures S17–S19, Supporting Information). First, the M—H_2O binding energy of Ni_{13} is close to that of Pt_{13}, but both are much higher than that of C—N. When the Ni_{13} nanoparticles are anchored on C—N, the M—H_2O binding energy increases significantly (Figure 4f; Figure S17, Supporting Information), accelerating the adsorption of H_2O and pushing the Volmer reaction toward the right side. Also, H_2O dissociation on Ni_{13}@C—N surface is only slightly higher than that on Pt_{13}, which is much lower than that on C—N surface. These results indicate that the dissociation of H_2O into H^+ and OH^- on Ni_{13}@C—N surface is fast, promoting a fast proton source supply for the HER. After dissociation, our DFT calculation shows that the M—H^+ binding energy with Ni_{13}@C—N is slightly lower than the ideal HER candidate Pt_{13} (Figure 4g; Figure S18, Supporting Information), and the OH^- binding energy is slightly higher (Figure 4h; Figure S19, Supporting Information). The moderate H^+ and OH^- binding energies could expedite the creation of M—H^+ and simultaneously refresh the active site on the Ni_{13}@C—N surface, improving the HER efficiency in alkaline solutions. Finally, the Gibbs free energy (ΔG_{H^*}) of HER of catalysts such as Ni_{13}@C—N, C—N, Pt_{13}, and Ni_{13} was further calculated by DFT to understand the high electrocatalytic activity (Figure 4i). The ΔG_{H^*} of Ni_{13}@C—N presented a relatively low negative Gibbs free energy than others, endowing its high electrocatalytic activity. This calculated mechanism is perfectly in line with our experimental results. It demonstrates that the strategy by anchoring Ni QD on C—N support can significantly improve the efficiency and kinetic of HER electrocatalytic to a level close to that of the expensive noble metal catalyst.

The mechanism of Ni@C—N nanocatalyst for HER and OER can be further discussed. The graphitized 3D C—N in the composite ply triple roles: a) the network provides a high surface area to interact with electrolyte; b) it provides the active sites required for the deposition and growth of Ni QD without aggregation or exfoliation; and c) it promotes the interelectron transport along with the interface of Ni@C—N between Ni nanocrystals and C—N. The Ni@C—N heterojunction with a tight connection between Ni nanocrystal and C—N offers a unique host–guest electronic interaction, which results in an electrically conductive path for fast electron transfer. The high catalytic activities can be attributed to the well-exposed active (111) crystal planes with comparable H_2O dissociation energy to Pt catalyst and appropriate binding energies with H_2O, H, and OH for Ni nanocrystal. Furthermore, the distance distribution of the Ni QD on the C—N support can allow the convection and release of H_2 and O_2 bubbles, reducing the damage of the catalysts by the high-pressure gas, and facilitate the gases recovery. In general, the Ni@C—N electrocatalyst could gain high HER and OER activities and stable long-term cycling capability thanks to the well-controlled synthesis method that took advantage of the naturally available deposition sites on life cells walls to regulate the growth of Ni QD and prevent their aggregation.

3. Conclusions

This work introduced Ni QD anchored on N-doped carbon derived from various biological sources as a bifunctional catalyst for HER and OER in water splitting. The prepared composite benefited from the abundant active sites on the cell walls and

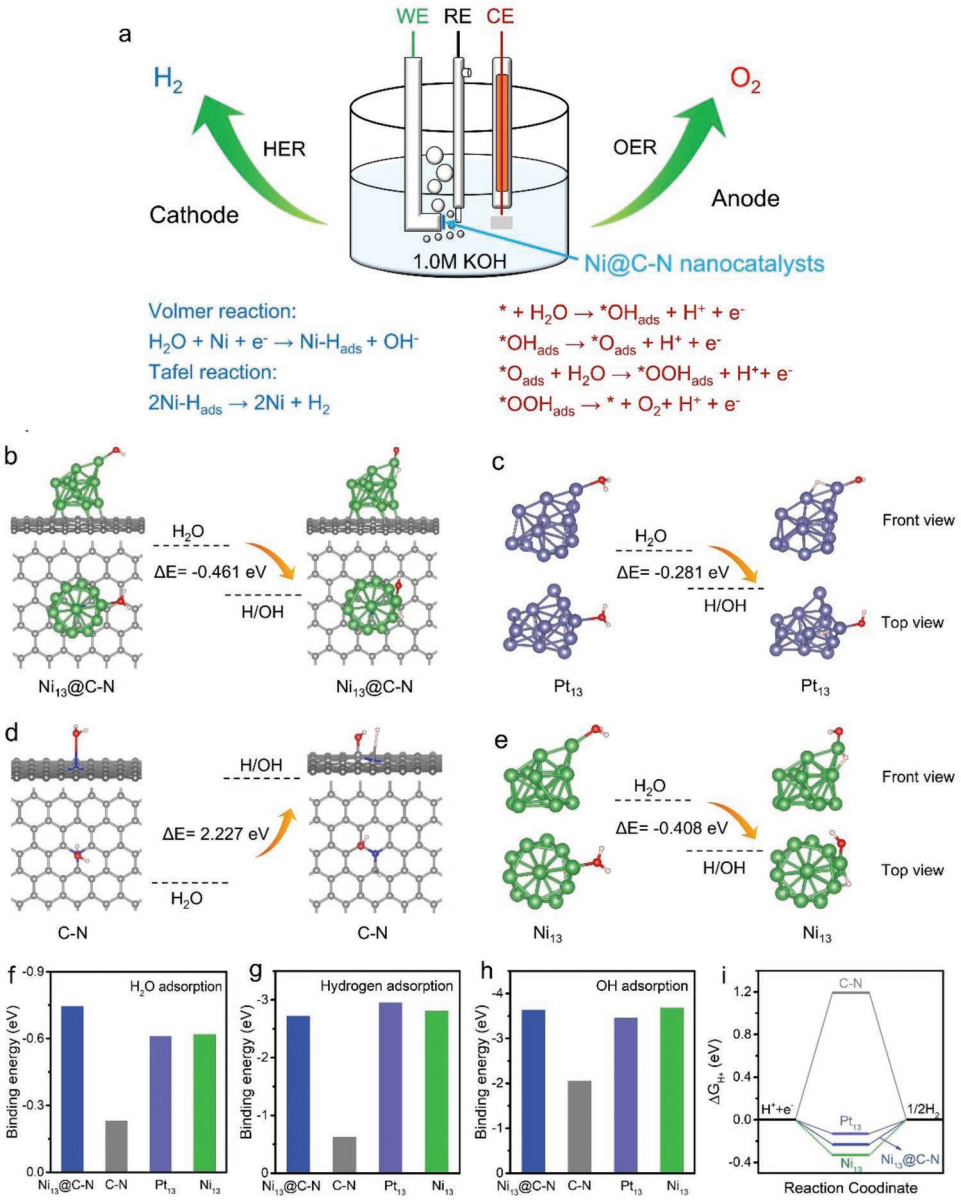

Figure 4. a) Detail water-splitting reactions and b–h) DFT calculations for HER reactivity of in alkaline solution. a–d) Adsorbed H_2O dissociation configuration on the surfaces: b) Ni_{13}@C–N, c) Pt_{13} nanoparticles, d) C–N, e) Ni_{13} nanoparticles, as well as their binding energies in alkaline solution. The green, gray, blue, purple, red, and ivory balls represent Ni, C, N, Pt, O, and H atoms, respectively. f) H_2O binding energies, g) H binding energies, and h) OH binding energies on the different surfaces of Ni_{13}@C–N, C–N, Pt_{13} nanoparticles, and Ni_{13} nanoparticles in alkaline solution. i) Reaction coordinate for HER, calculating ΔG_{H^*} for atomic H adsorption on Ni_{13}@C–N, C–N, Pt_{13}, and Ni_{13}.

membranes in plants cell to homogeneously deposited Ni^+ and consequently discharge it to Ni. By controlling the amount of the Ni precursor, the growth of Ni particles was limited to give QD. The distance between the initial Ni seed sites prevented the Ni QD from aggregation and/or agglomeration. When the green Ni–biomass precursor was heat-treated at 800 °C, the biomass was converted to 3D porous graphitized carbon doped with nitrogen, while the Ni compound was reduced to metallic Ni QD (about 3–4 nm in size). The heat treatment also helped to strengthen the bond between Ni QD and the N-doped carbon substrate. The well-designed composite wetted well with water and has a high surface area with enormous catalytically active sites and rapid charge-transfer capability. As a result, the Ni@C–N–AG composite exhibits excellent stability and HER and OER activities in 1.0 M KOH alkaline electrolyte. The Ni@C–N–AG needed 170 and 319 mV overpotentials to reach the current density of 10 mA cm^{-2} for HER and OER, respectively, comparable with the expensive noble-metal-based bifunctional electrocatalysts. The DFT calculation investigated the HER mechanism, which suggested that the well-exposed active (111) crystal planes of Ni QD have a relatively low negative Gibbs free energy for HER that is very close to that of Pt catalyst. The DFT calculations also proved that the binding energies between Ni QD surface and H_2O, H, and OH are also close to that reported

for Pt electrode. We believe that the design of the hybrid electrocatalysts is universal and could be used to synthesis similar QD–carbon as stable bifunctional electrocatalysts for water-splitting and other electrocatalysis reactions.

4. Experimental Section

Chemicals and Raw Materials: The biomass materials, including AG, WR, and PT, were purchased from the supermarket. $Ni(NO_3)_2{\cdot}6H_2O$, KOH, and Milli-Q ultrapure water (Millipore, ≥18.2 MΩ cm) were purchased from Shanghai DeNA. The Nafion solution (5 wt%, D520), deionized water, and absolute ethanol were purchased from Shanghai Hesen. All chemical reagents were of analytical grade.

Synthesis of Ni@C—N Nanocatalysts: The biomass materials were cut into small cubes and impregnated with $Ni(NO_3)_2{\cdot}6H_2O$ aqueous solutions with different concentrations (0.1, 0.2, 0.3, 0.4, and 0.5 M) 2 h. To maintain the biochar materials' morphological integrity and ionic dispersion, all the macerated samples were placed in a freeze-dryer to obtain the composite precursors. After freeze-drying, the as-obtained precursors were further annealed at different temperatures (400, 500, 600, 700, 800, and 900 °C) in Ar atmosphere for 2 h with a heating rate of 2 °C min^{-1}. Different samples were prepared using a similar method, and the abbreviations of these materials are listed in Table S1 (Supporting Information).

Characterization: The powder XRD patterns were recorded at room temperature by a diffractometer (AXS D8 Advance, Bruker) equipped with a Cu Kα radiation. The morphology and composition of the prepared catalysts were characterized by scanning electron microscopy (SEM, JSM-7001F, JEOL) equipped with an EDS microanalyzer (QUANTAX EDS, Bruker). The structure and morphology of the as-prepared composite nanoparticles were further studied by TEM (Tecnai G2 F30 S-TWIN, FEI), HRTEM, and SAED. Nano Measurer calculated the size distribution of Ni nanoparticles. Raman spectroscopies (HORIBA LabRAM HR Evolution instrument) were carried out under the excitation at 532 nm. XPS data were collected via an X-ray photoelectron spectrometer (ESCALAB 250XI, Thermo). ICP-OES was performed on an Agilent 5110 instrument. The Brunauer–Emmett–Teller (BET) surface areas of the prepared materials were measured on an ASAP 2020 physisorption analyzer (Micromeritics Instrument Corporation).

Electrochemical Tests: The electrochemical measurements, e.g., linear sweep voltammetry (LSV), were carried out on a three-electrode system in 1.0 M KOH at 25 °C, connecting with an electrochemical workstation (CHI660E). A Pt slice was used as a counter electrode, while an Ag/AgCl electrode with saturated KCl and a glassy carbon electrode (GCE) were selected as the reference and working electrodes, respectively. All potentials versus Ag/AgCl reported herein were converted to the reversible hydrogen electrode (RHE) with the Nernst equation ($E_{RHE} = E_{Ag/AgCl} + 0.059\ pH + 0.197$). All polarization curves were *IR*-corrected with 90% *IR* compensation. The overpotential for OER is calculated by η (V) = $E_{RHE} - 1.23$ V. The catalytic dispersions or inks were prepared by mixing 5 mg catalyst in a 1 mL solution mixture containing 750 µL of ethanol, 200 µL of ultrapure water (DeNA), and 50 µL of the Nafion solution (5 wt%, D520). The mixture was sonicated for at least 30 min to form a homogeneous solution and deposited on a freshly polished GCE (diameter = 5 mm).

Density Functional Theory Calculation: Based on the DFT, the Vienna ab initio simulation package (VASP) was used in all calculations.[62–64] The exchange–correlation interactions were applied using the generalized gradient approximation of the Perdew–Burke–Ernzerhof functional (PBE type).[65,66] The plane-wave cutoff energy was set to 400 eV, and the Brillouin-zone integration was set to a *k*-mesh of 3 × 3 × 3. The energy convergence criterion for atomic structures was 10^{-4} eV $atom^{-1}$, and the convergence threshold for the forces was 0.01 eV $Å^{-1}$. To avoid interactions between neighboring slices due to lattice periodicity, a vacuum slab of 15 Å was introduced in the *z*-direction. The influence of van der Waals interactions was considered by using the vdW-D3 method.

The Gibbs free energy (ΔG) for HER was also calculated. The formulae for H adsorption on the surface of catalysts are as follows[67]

$$\Delta E_{H^*} = E_{(H^*Slab)} - E_{(Slab)} - 1/2E_{(H2)} \quad (1)$$

$$\Delta G_{H^*} = \Delta E_{H^*} + \Delta E_{ZPE} - T\Delta S \quad (2)$$

where $E_{(H^*Slab)}$ is the energy of the total system with absorbing individual hydrogen atoms, $E_{(Slab)}$ is the pure surface energy, and $E_{(H_2)}$ is the hydrogen molecules energy. ΔE_{ZPE} is the zero-point energy, and $T\Delta S$ is the change of entropy (T = 298.15 K).

Supporting Information

Supporting Information is available from the Wiley Online Library or from the author.

Acknowledgements

This work was financially supported by the Open Foundation of State Key Laboratory of Mineral Processing (BGRIMM-KJSKL-2021-11), the Engineering Research Center of Non-metallic Minerals of Zhejiang Province (Grant No. ZD2020K04), the Fundamental Research Funds for the Central Universities (Grant Nos. 2652019164 and 2652019033), and the National Natural Science Foundation of China (Grant No. 5217042069).

Conflict of Interest

The authors declare no conflict of interest.

Author Contributions

S.C. and X.M. contributed equally to this work. S.C. contributed in methodology, validation, formal analysis, investigation, writing the original draft, data curation, and visualization. X.M. contributed in conceptualization, methodology, supervision, project administration, writing—review and editing, funding acquisition, and resources. Y.Z. contributed in methodology, investigation, and formal analysis. X.X.W. contributed in investigation and formal analysis. D.Z. contributed in data discussion. X.F. contributed in investigation. X.W.W. contributed in investigation. Y.L. contributed in investigation, and writing the review and editing. Z.H. contributed in writing the review and editing, and resources. A.M.A. contributed in writing the review and editing, and resources. K.X. contributed in formal analysis, data discussion, and writing the review and editing. M.F. contributed in conceptualization, supervision, writing the review and editing, project administration, and funding acquisition.

Data Availability Statement

Research data are not shared.

Keywords

bifunctional electrocatalysts, density functional theory, N-doped carbon, nickel nanocrystals, overall water splitting

Received: October 15, 2021
Revised: November 11, 2021
Published online: January 7, 2022

[1] N. Han, P. Liu, J. Jiang, L. Ai, Z. Shao, S. Liu, *J. Mater. Chem. A* **2018**, *6*, 19912.
[2] U. Gupta, C. Rao, *Nano Energy* **2017**, *41*, 49.
[3] X. Du, J. Huang, J. Zhang, Y. Yan, C. Wu, Y. Hu, C. Yan, T. Lei, W. Chen, C. Fan, *Angew. Chem., Int. Ed.* **2019**, *58*, 4484.
[4] I. Roger, M. A. Shipman, M. D. Symes, *Nat. Rev. Chem.* **2017**, *1*, 1.
[5] Q. Hu, G. Li, G. Li, X. Liu, B. Zhu, X. Chai, Q. Zhang, J. Liu, C. He, *Adv. Energy Mater.* **2019**, *9*, 1803867.
[6] Y. P. Zhu, C. Guo, Y. Zheng, S.-Z. Qiao, *Acc. Chem. Res.* **2017**, *50*, 915.
[7] R. Wu, B. Xiao, Q. Gao, Y. R. Zheng, X. S. Zheng, J. F. Zhu, M. R. Gao, S. H. Yu, *Angew. Chem.* **2018**, *130*, 15671.
[8] Y. Jiao, Y. Zheng, M. Jaroniec, S. Z. Qiao, *Chem. Soc. Rev.* **2015**, *44*, 2060.
[9] Z. Cai, X. Bu, P. Wang, J. C. Ho, J. Yang, X. Wang, *J. Mater. Chem. A* **2019**, *7*, 5069.
[10] H. Zhou, F. Yu, J. Sun, R. He, S. Chen, C.-W. Chu, Z. Ren, *Proc. Natl. Acad. Sci. USA* **2017**, *114*, 5607.
[11] J. Wang, F. Xu, H. Jin, Y. Chen, Y. Wang, *Adv. Mater.* **2017**, *29*, 29.
[12] X. Zou, Y. Zhang, *Chem. Soc. Rev.* **2015**, *44*, 5148.
[13] S. Lin, H. Wang, F. Wu, Q. Wang, X. Bai, D. Zu, J. Song, D. Wang, Z. Liu, Z. Li, N. Tao, K. Huang, M. Lei, B. Li, H. Wu, *npj Flexible Electron.* **2019**, *3*, 6.
[14] S. Lin, X. Bai, H. Wang, H. Wang, J. Song, K. Huang, C. Wang, N. Wang, B. Li, M. Lei, H. Wu, *Adv. Mater.* **2017**, *29*, 1703238.
[15] S. Lin, H. Wang, X. Zhang, D. Wang, D. Zu, J. Song, Z. Liu, Y. Huang, K. Huang, N. Tao, Z. Li, X. Bai, B. Li, M. Lei, Z. Yu, H. Wu, *Nano Energy* **2019**, *62*, 111.
[16] Y. Zhao, X. Min, Z. Ding, S. Chen, C. Ai, Z. Liu, T. Yang, X. Wu, Y. g. Liu, S. Lin, Z. Huang, P. Gao, H. Wu, M. Fang, *Adv. Sci.* **2019**, *7*, 1902051.
[17] Y. Hou, M. R. Lohe, J. Zhang, S. Liu, X. Zhuang, X. Feng, *Energy Environ. Sci.* **2016**, *9*, 478.
[18] D. S. Raja, H.-W. Lin, S.-Y. Lu, *Nano Energy* **2019**, *57*, 1.
[19] H. Sun, J.-G. Li, L. Lv, Z. Li, X. Ao, C. Xu, X. Xue, G. Hong, C. Wang, *J. Power Sources* **2019**, *425*, 138.
[20] M. Yao, B. Sun, N. Wang, W. Hu, S. Komarneni, *Appl. Surf. Sci.* **2019**, *480*, 655.
[21] W. Zhen, J. Ma, G. Lu, *Appl. Catal., B* **2016**, *190*, 12.
[22] Y. Shi, B. Zhang, *Chem. Soc. Rev.* **2016**, *45*, 1529.
[23] M. Ledendecker, S. K. Calderon, C. Papp, H.-P. Steinrueck, M. Antonietti, M. Shalom, *Angew. Chem., Int. Ed.* **2015**, *54*, 12361.
[24] X. He, S. Z. Luan, L. Wang, R. Y. Wang, P. Du, Y. Y. Xu, H. J. Yang, Y. G. Wang, K. Huang, M. Lei, *Mater. Lett.* **2019**, *244*, 78.
[25] J. Luo, J.-H. Im, M. T. Mayer, M. Schreier, M. K. Nazeeruddin, N.-G. Park, S. D. Tilley, H. J. Fan, M. Grätzel, *Science* **2014**, *345*, 1593.
[26] H. Wang, H.-W. Lee, Y. Deng, Z. Lu, P.-C. Hsu, Y. Liu, D. Lin, Y. Cui, *Nat. Commun.* **2015**, *6*, 7261.
[27] M. Gong, W. Zhou, M.-C. Tsai, J. Zhou, M. Guan, M.-C. Lin, B. Zhang, Y. Hu, D.-Y. Wang, J. Yang, S. J. Pennycook, B.-J. Hwang, H. Dai, *Nat. Commun.* **2014**, *5*, 4695.
[28] X. He, S. Luan, L. Wang, R. Wang, P. Du, Y. Xu, H. Yang, Y. Wang, K. Huang, M. Lei, *Mater. Lett.* **2019**, *244*, 78.
[29] D. Zhang, H. Mou, F. Lu, C. Song, D. Wang, *Appl. Catal., B* **2019**, *254*, 471.
[30] C.-N. Lv, L. Zhang, X.-H. Huang, Y.-X. Zhu, X. Zhang, J.-S. Hu, S.-Y. Lu, *Nano Energy* **2019**, *65*, 103995.
[31] S. Anantharaj, S. R. Ede, K. Sakthikumar, K. Karthick, S. Mishra, S. Kundu, *ACS Catal.* **2016**, *6*, 8069.
[32] X. Liu, X. Wang, X. Yuan, W. Dong, F. Huang, *J. Mater. Chem. A* **2016**, *4*, 167.
[33] Y. Xu, W. Tu, B. Zhang, S. Yin, Y. Huang, M. Kraft, R. Xu, *Adv. Mater.* **2017**, *29*, 1605957.
[34] X. Wang, L. Yu, B. Y. Guan, S. Song, X. W. Lou, *Adv. Mater.* **2018**, *30*, 1801211.
[35] J. Nai, J. Zhang, X. W. D. Lou, *Chem* **2018**, *4*, 1967.
[36] S. M. Lama, J. Pampel, T.-P. Fellinger, V. P. Beškoski, L. Slavković-Beškoski, M. Antonietti, V. Molinari, *ACS Sustainable Chem. Eng.* **2017**, *5*, 2415.
[37] M. Li, Y. Zhu, N. Song, C. Wang, X. Lu, *J. Colloid Interface Sci.* **2018**, *514*, 199.
[38] X. Lu, F. Yu, L. Lou, X. W. D. Lou, *Sci. Adv.* **2019**, *5*, eaav6009.
[39] H. Jin, J. Wang, D. Su, Z. Wei, Z. Pang, Y. Wang, *J. Am. Chem. Soc.* **2015**, *137*, 2688.
[40] Z.-Y. Wu, W.-B. Ji, B.-C. Hu, H.-W. Liang, X.-X. Xu, Z.-L. Yu, B.-Y. Li, S.-H. Yu, *Nano Energy* **2018**, *51*, 286.
[41] W. Zhang, X. Zhang, L. Chen, J. Dai, Y. Ding, L. Ji, J. Zhao, M. Yan, F. Yang, C.-R. Chang, *ACS Catal.* **2018**, *8*, 8092.
[42] H.-W. Liang, S. Brüller, R. Dong, J. Zhang, X. Feng, K. Müllen, *Nat. Commun.* **2015**, *6*, 7992.
[43] Z. Y. Wu, X. X. Xu, B. C. Hu, H. W. Liang, Y. Lin, L. F. Chen, S. H. Yu, *Angew. Chem.* **2015**, *127*, 8297.
[44] P. Su, K. Iwase, S. Nakanishi, K. Hashimoto, K. Kamiya, *Small* **2016**, *12*, 6083.
[45] K. R. Zhu, C. L. Chen, S. H. Lu, X. D. Zhang, A. Alsaedi, T. Hayat, *Carbon* **2019**, *148*, 52.
[46] J. H. Lehman, M. Terrones, E. Mansfield, K. E. Hurst, V. Meunier, *Carbon* **2011**, *49*, 2581.
[47] C. Lei, Y. Wang, Y. Hou, P. Liu, J. Yang, T. Zhang, X. Zhuang, M. Chen, B. Yang, L. Lei, C. Yuan, M. Qiu, X. Feng, *Energy Environ. Sci.* **2019**, *12*, 149.
[48] S. A. Abbas, M. I. Iqbal, S.-H. Kim, K.-D. Jung, *Electrochim. Acta* **2017**, *227*, 382.
[49] R. Li, X. Li, D. Yu, L. Li, G. Yang, K. Zhang, S. Ramakrishna, L. Xie, S. Peng, *Carbon* **2019**, *148*, 496.
[50] X. Min, B. Sun, S. Chen, M. Fang, X. Wu, Y. g. Liu, A. Abdelkader, Z. Huang, T. Liu, K. Xi, R. Vasant Kumar, *Energy Storage Mater.* **2019**, *16*, 597.
[51] T. Wang, Y. Sun, A. Li, Y. Ma, D. Feng, Y. Fang, Y. Liu, Q. Huo, Z.-A. Qiao, S. Dai, *RSC Adv.* **2017**, *7*, 50966.
[52] H. Fei, J. Dong, M. J. Arellano-Jiménez, G. Ye, N. D. Kim, E. L. Samuel, Z. Peng, Z. Zhu, F. Qin, J. Bao, M. J. Yacaman, P. M. Ajayan, D. Chen, J. M. Tour, *Nat. Commun.* **2015**, *6*, 8668.
[53] Z. Zhuang, S. A. Giles, J. Zheng, G. R. Jenness, S. Caratzoulas, D. G. Vlachos, Y. Yan, *Nat. Commun.* **2016**, *7*, 10141.
[54] J. Ren, M. Antonietti, T. P. Fellinger, *Adv. Energy Mater.* **2015**, *5*, 1401660.
[55] L. Fan, P. F. Liu, X. Yan, L. Gu, Z. Z. Yang, H. G. Yang, S. Qiu, X. Yao, *Nat. Commun.* **2016**, *7*, 10667.
[56] H. Yu, Y. Xue, L. Hui, C. Zhang, Y. Li, Z. Zuo, Y. Zhao, Z. Li, Y. Li, *Adv. Mater.* **2018**, *30*, 1707082.
[57] W. Sun, L. Du, C. Du, Y. Gao, G. Yin, *Appl. Surf. Sci.* **2019**, *485*, 41.
[58] W. Zhang, Y. Li, X. Zeng, S. Peng, *Sci. Rep.* **2015**, 1.
[59] J. Wang, Y. Gao, T. L. You, F. Ciucci, *J. Power Sources* **2018**, *401*, 312.
[60] T. Dong, X. Zhang, P. Wang, H.-S. Chen, P. Yang, *Carbon* **2019**, *149*, 222.
[61] S. Diaz-Coello, G. Garcia, M. C. Arevalo, E. Pastor, *Int. J. Hydrogen Energy* **2019**, *44*, 12576.
[62] G. Kresse, D. Joubert, *Phys. Rev. B* **1999**, *59*, 1758.
[63] P. E. Blöchl, *Phys. Rev. B* **1994**, *50*, 17953.
[64] G. Kresse, J. Furthmüller, *Phys. Rev. B* **1996**, *54*, 11169.
[65] J. P. Perdew, K. Burke, M. Ernzerhof, *Phys. Rev. Lett.* **1996**, *77*, 3865.
[66] Y. Zhang, W. Yang, *Phys. Rev. Lett.* **1998**, *80*, 890.
[67] J. K. Nørskov, T. Bligaard, A. Logadottir, J. Kitchin, J. G. Chen, S. Pandelov, U. Stimming, *J. Electrochem. Soc.* **2005**, *152*, J23.